RSC Advances

PAPER

View Article Online
View Journal | View Issue

Cite this: *RSC Adv.*, 2025, **15**, 28358

Mechanical performance and aging resistance analysis of zinc oxide-reinforced polyurethane composites†

Chien-Chiang Tung,‡[a] Yen-Hong Lin, ‡[b] Yi-Wen Chen *[bcd] and Fu-Ming Wang *[a]

Herein, we report the development of three-dimensional (3D)-printed polyurethane (PU) composite materials reinforced with zinc oxide (ZnO) nanoparticles and stabilised *via* surface functionalization using the silane coupling agent 3-(trimethoxysilyl)propyl methacrylate (TMSPM). By employing digital light processing (DLP) technology, a series of porous PU scaffolds containing different concentrations of ZnO (0, 1, and 2 wt%) were successfully fabricated. The primary objective was to enhance the mechanical integrity and environmental durability of PU-based components, particularly under ultraviolet (UV) exposure and thermal aging. The inclusion of the TMSPM-modified ZnO nanoparticles significantly improved the homogeneity of the nanoparticle dispersion and the interfacial compatibility between the inorganic fillers and the polymeric matrix. Compared to the control group, ZnO-reinforced scaffolds exhibited up to 53% higher compressive strength and retained over 75% of their mechanical performance after 150 hours of UV and thermal aging. Surface contact angles also increased significantly upon aging, reaching values above 90°, suggesting altered surface morphology and reduced moisture affinity. Additionally, microstructural analysis revealed that ZnO incorporation mitigated the formation of surface cracks and delamination during aging, preserving the structural continuity of the scaffolds. These enhancements are ascribed to the synergistic effects of the ZnO nanofillers, which function as effective UV radiation absorbers and physical barriers that suppress microcrack initiation and propagation within the polymer network. This study demonstrates a viable strategy for improving the long-term performance and structural reliability of 3D-printed PU components by incorporating silane-functionalised ceramic nanofillers. The resulting PU/TMSPM–ZnO nanocomposites are promising for lightweight, mechanically resilient, and aging-resistant applications across a range of sectors, including automotive, aerospace, and outdoor structural engineering.

Received 28th May 2025
Accepted 4th July 2025

DOI: 10.1039/d5ra03748d

rsc.li/rsc-advances

1. Introduction

Additive manufacturing (AM) has profoundly transformed modern fabrication technologies by enabling the production of geometrically complex and structurally efficient components with unprecedented design flexibility and material utilisation.[1–4] This transformative capability is particularly relevant in the automotive and aerospace sectors, where strict demands for lightweight performance, energy efficiency, and environmental durability drive material innovation. Within the broad landscape of AM techniques, digital light processing (DLP)-based three-dimensional (3D) printing stands out for its high spatial resolution, rapid prototyping capabilities, and ability to precisely cure photopolymer resins, facilitating the layer-by-layer construction of polymeric components with customisable architectures and mechanical functionalities.[5–8] Among the diverse classes of photopolymers, polyurethane (PU) has emerged as a promising candidate owing to its versatility as a thermosetting elastomer.[9–11] It exhibits advantageous properties, such as high elasticity, abrasion resistance, biocompatibility, and resistance to oils and solvents, which have led to its widespread use in applications ranging from biomedical scaffolds and protective coatings to automotive interior parts and energy-absorbing structures.[12] However, despite its favourable mechanical performance and processability, PU suffers from inherent limitations when exposed to prolonged ultraviolet (UV)

---

[a] *Graduate Institute of Applied Science and Technology, National Taiwan University of Science and Technology, Taipei 10607, Taiwan. E-mail: mccabe@mail.ntust.edu.tw*

[b] *Research & Development Center for x-Dimensional Extracellular Vesicles, China Medical University Hospital, Taichung 404327, Taiwan. E-mail: evinchen@mail.cmu.edu.tw*

[c] *Graduate Institute of Biomedical Sciences, China Medical University, Taichung 406040, Taiwan*

[d] *Department of Bioinformatics and Medical Engineering, Asia University, Taichung 41354, Taiwan*

† Electronic supplementary information (ESI) available. See DOI: https://doi.org/10.1039/d5ra03748d

‡ Chien-Chiang Tung and Yen-Hong Lin contributed equally to this work.

irradiation and oxidative conditions.[13] Under such environmental stressors, photooxidative degradation of urethane linkages results in polymer chain scission, yellowing, embrittlement, surface cracking, and a progressive decline in load-bearing capacity. These age-related degradations severely hinder the use of PU in high-performance outdoor structural applications, necessitating the development of novel material modification strategies to mitigate degradation while preserving mechanical integrity.

A significant body of research has explored the use of nanofillers as functional reinforcements to improve the mechanical thermal properties and aging resistance of polymer composites.[14] Zinc oxide (ZnO) nanoparticles, characterised by their wide bandgap (∼3.3 eV), potent UV-blocking capacity, intrinsic antimicrobial properties, and high thermal stability, have emerged as promising additives for improving the photostability and durability of polymeric systems.[15] ZnO can act as both a physical UV shield and a radical scavenger, delaying the onset of photodegradation in the matrix.[16] However, the nanoscale dimensions of ZnO and its high surface energy predispose it to agglomeration within organic matrices, leading to nonuniform dispersion and compromised mechanical reinforcement.[17] Surface functionalization techniques have been widely investigated to address the dispersion challenges and ensure efficient interfacial load transfer.[18] Among these, silane coupling agents, such as 3-(trimethoxysilyl)propyl methacrylate (TMSPM), offer dual functionality: the methacrylate moiety participates in free-radical polymerisation with acrylate-based resins during DLP processing, while the trialkoxysilane group forms strong covalent bonds with hydroxylated inorganic surfaces, such as ZnO nanoparticles.[19,20] This chemical bridging enhances the nanoparticle dispersion and integration within the polymer network. Previous reports have shown that TMSPM-modified fillers can improve the stiffness, dimensional stability, and weathering resistance of thermoset matrices while maintaining optical clarity and hydrophobicity.[21,22] Despite these advantages, the combined use of TMSPM and ZnO in light-curable PU systems remains underexplored, particularly in the context of additively manufactured architectures.

To date, most investigations involving TMSPM–ZnO hybrids have been limited to cast films or thermally cured composites, leaving a gap in the understanding of their behaviour in photopolymerization and layered 3D printing environments.[23] Few studies have simultaneously evaluated the effects of silane-modified ZnO on the aging resistance, mechanical performance, and microstructural fidelity of 3D-printed PU materials. As AM transitions from prototyping to direct end-use production, the durability of hybrid nanocomposites under real-world service conditions has become a vital concern. We have previously demonstrated that coating 3D-printed PU scaffolds with polydopamine and graphene significantly improved their resistance to UV degradation and enhanced their compressive strength by facilitating uniform stress distribution and radical quenching.[24] Building on this foundational strategy, this study introduces a bulk reinforcement approach that directly integrates TMSPM-functionalised ZnO nanoparticles in a PU matrix. This design combines the benefits of nanoparticle-mediated UV shielding with improved filler–matrix interactions *via* silane chemistry, thus achieving a well-dispersed, high-performance composite system.

In this study, we report the formulation, 3D printing, and comprehensive characterisation of a series of DLP-fabricated PU scaffolds embedded with varying concentrations of TMSPM-modified ZnO nanoparticles. The nanocomposite scaffolds were systematically evaluated for their structural morphology, surface wettability, thermal degradation profiles, and accelerated UV aging resistance. The mechanical performance under compressive stress was quantified to assess the reinforcement efficiency at different filler loadings. The results of this study provide new insights into the structure–property–processing relationships governing silane-grafted ZnO nanocomposites and offer a scalable strategy for fabricating lightweight, durable, and environmentally resilient polymeric materials tailored for the transportation, aerospace, and other performance-critical sectors.

2. Experimental

2.1. Materials and reagents

Photocurable waterborne PU was obtained from Alberdingk Boley (Krefeld, Germany). 2-Hydroxyethyl methacrylate (HEMA), 3-(trimethoxysilyl)propyl methacrylate (TMSPM), and zinc oxide (ZnO) nanoparticles were purchased from Sigma-Aldrich (St. Louis, MO, USA). The photoinitiator 2,4,6-trimethylbenzoyl-diphenylphosphine oxide (TPO) was acquired from Ciba Specialty Chemicals (Basel, Switzerland). All chemicals were used as received without further purification. Deionized water was used for all aqueous preparations.

2.2. Preparation of photocurable PU composite resin

Photocurable water-based PU resin was first heated at 80 °C to partially remove water content until the resin reached approximately 60% of its original weight. After cooling to room temperature, 30 wt% of HEMA, and 1.5 wt% of TPO were added as the reactive diluent and photoinitiator, respectively. The mixture was stirred homogeneously in a dark environment. Subsequently, 2 wt% of TMSPM was incorporated as a silane coupling agent to promote interfacial compatibility with ZnO nanoparticles. For experimental groups, ZnO nanoparticles were added at concentrations of 0, 1, or 2 wt% (denoted as Z0, Z1, and Z2) relative to the total solid content. The resulting

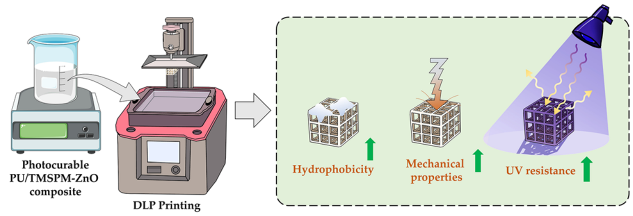

Fig. 1 Schematic diagram of PU scaffold fabrication incorporating TMSPM-modified ZnO for improved mechanical performance and environmental aging resistance.

formulations were ultrasonicated to ensure uniform nanoparticle dispersion and stored in the dark to prevent premature curing. The conceptual overview in Fig. 1 outlines the combined use of ZnO surface functionalization and DLP-based 3D printing, aiming to enhance scaffold performance in terms of wettability, mechanical integrity, and UV durability. The detailed materials preparation and characterization procedures are described in the following sections.

2.3. Rheological characterization

The viscosity of the photocurable PU composite resin was evaluated using a modular compact rheometer (MCR302, Anton Paar, Graz, Austria). 300 μL of each composite was loaded onto the lower plate. A steady shear test was performed at 25 °C, and the viscosity was recorded over a shear rate range of 0.1–1000 s^{-1}. All measurements were conducted in triplicate to ensure reproducibility.

2.4. Fabrication of 3D-printed PU/TMSPM–ZnO structures

The prepared PU/TMSPM–ZnO composite resins were printed into lattice-structured scaffolds using a DLP 3D printer (Miicraft Ultra 50, Young Optics Inc., Taiwan) equipped with a 405 nm UV light source. The scaffold model was designed as a lattice structure with dimensions of $5 \times 5 \times 6.2$ mm^3, featuring a uniform pore size of 1 mm and a strut thickness of 0.5 mm. A three-layer buffer layer and 1 mm gap layer were included, and a single-layered base layer was applied to ensure proper adhesion to the build platform. During printing, the build layer thickness was set to 100 μm with a 7–9.5 s exposure time per layer to ensure the complete polymerisation of each layer. The first (bottom) layer was exposed for 8.5–12 s to improve base adhesion. The printed scaffolds were thoroughly rinsed with ethanol to remove residual uncured resin and then post-cured under a 405 nm UV lamp for 10 min to enhance crosslinking and dimensional stability. The samples were stored in a desiccator until further testing.

2.5. Chemical structure analysis

Fourier transform infrared spectroscopy (FTIR; Nicolet 6700, Thermo Fisher Scientific, USA) was used to examine the chemical interactions and functional groups within the PU/TMSPM–ZnO composites. The samples were analysed in attenuated total reflectance (ATR) mode over the range of 4000–600 cm^{-1} with a resolution of 4 cm^{-1} and 32 scans per spectrum. The spectra were collected before and after accelerated aging to assess the chemical changes induced by UV exposure.

2.6. Crystallographic characterization

X-ray diffraction (XRD) patterns of the PU/TMSPM–ZnO composites were obtained using a powder X-ray diffractometer (D8 Advance, Bruker, Germany) equipped with a Cu Kα radiation source ($\lambda = 1.5406$ Å) operating at 40 kV and 40 mA. Scans were conducted in the 2θ range of 20°–50° with a step size of 1°.

2.7. Surface wettability evaluation

The surface wettability of the PU/TMSPM–ZnO composites was evaluated *via* static water contact angle measurements using a goniometer (SmartDrop, Femtobiomed, Korea). A 5 μL droplet of deionised water was deposited onto the surface of each sample, and the contact angle was measured within 10 s using image analysis software. Five replicates ($n = 5$) were tested and averaged for each group. Measurements were performed before and after accelerated aging to assess changes in hydrophilicity or surface energy.

2.8. Surface morphology and elemental mapping

The surface morphology and dispersion state of the ZnO nanoparticles within the printed scaffolds were examined using field-emission scanning electron microscopy (FE-SEM; JSM-7800F, JEOL, Japan). Samples were sputter-coated with platinum for 60 s prior to imaging. To confirm the presence and uniformity of ZnO in the PU matrix, elemental distribution analysis using energy-dispersive X-ray spectroscopy (EDX) mapping was performed at an accelerating voltage of 15 kV.

2.9. Compressive mechanical testing

The mechanical performance of the printed PU/TMSPM–ZnO scaffolds was evaluated *via* uniaxial compression testing using a universal testing machine (EZ-Test, Shimadzu, Japan). Compression tests were performed at a crosshead speed of 1 mm min^{-1} with the loading axis aligned perpendicular to the top surface of the scaffold. The compressive modulus was calculated from the initial linear region of the stress–strain curve. For each group, six samples ($n = 6$) were tested both before and after aging to assess the effect of the ZnO content and environmental exposure on the mechanical integrity and structural retention.

2.10. Environmental durability evaluation

To evaluate the environmental durability of the printed PU/TMSPM–ZnO scaffolds, an accelerated aging test was performed using alternating cycles of UV irradiation and thermal exposure. Each cycle consisted of 10 h of UV exposure followed by 10 h of heating. UV exposure (254 nm) was conducted in a sterile laminar flow cabinet typically used for cell culture (Thermo Scientific), while thermal exposure was performed in a conventional laboratory oven maintained at 80 °C. In addition, freeze–UV alternating cycles involving −80 °C freezing and UV exposure at room temperature were performed, and results are provided in the ESI.† Samples were collected after cumulative exposure times of 50, 100, and 150 h. At each time point, the specimens were subjected to the aforementioned physical and chemical analyses to evaluate the effects of aging on material performance and structural stability.

2.11. Statistical analysis

All quantitative data are presented as mean ± standard deviation (SD). Statistical comparisons between groups were performed using one-way analysis of variance (ANOVA), followed by

Scheffé's post hoc test for multiple comparisons. Statistical significance was set at $p < 0.05$.

3. Results

3.1. Scaffold design and visual appearance

The PU-based scaffolds exhibited precise replication of the designed lattice geometry, with interconnected pores and uniform strut dimensions across all groups (Z0, Z1, and Z2). The as-printed Z0 samples exhibited a transparent yellowish appearance, which is characteristic of the base PU/HEMA matrix. Upon the incorporation of ZnO nanoparticles, the colour of the scaffolds gradually shifted toward opaque white with increasing filler content. Specifically, the Z1 group displayed a semi-translucent, milky-white hue, whereas the Z2 group exhibited a fully opaque white colouration. To further understand the effects of ZnO incorporation on resin behavior, rheological measurements were conducted. As shown in Fig. 2A, all resin formulations demonstrated shear-thinning behavior, where viscosity decreased with increasing shear rate. The addition of ZnO significantly elevated the overall viscosity, with Z2 exhibiting the highest values throughout the range. Despite this increase, the viscosities remained within a printable range under high shear conditions relevant to DLP processes. Fig. 2B presents the shear stress–strain relationship, where Z1 and Z2 displayed steeper slopes compared to Z0, indicating enhanced resistance to shear deformation, likely due to filler-induced matrix stiffening and improved network entanglement. Visual inspection of the resins (Fig. 2C) also revealed differences in opacity, with Z0 remaining nearly transparent, Z1 exhibiting moderate cloudiness, and Z2 becoming highly opaque. After printing and curing, the color differences remained evident in the final scaffolds (Fig. 2D and E), reflecting the embedded filler concentration and dispersion. Despite these visual and rheological differences, all groups were successfully printed with high fidelity using adjusted exposure parameters to compensate for filler-induced UV attenuation. The morphological characteristics of the TMSPM-modified ZnO nanoparticles are presented in Fig. S1.† SEM analysis revealed that the nanoparticles exhibit irregular prismatic shapes with an average diameter of approximately 200 ± 50 nm.

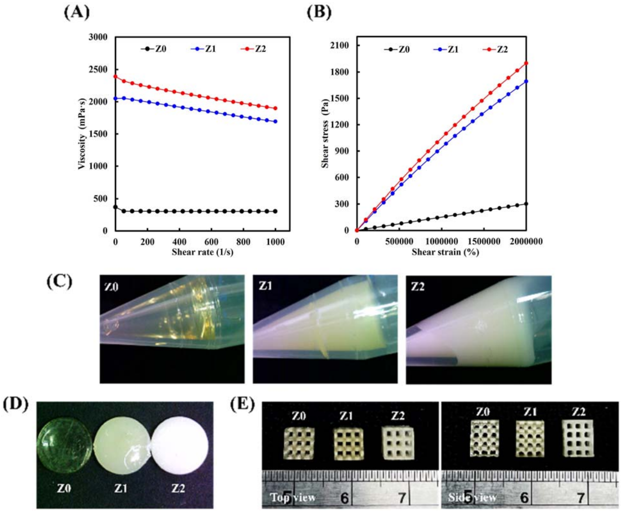

Fig. 2 (A) Viscosity profiles of Z0, Z1, and Z2 resin formulations measured over a range of shear rates. (B) Shear stress–strain curves of each formulation. (C) Resin appearance in conical tubes after UV exposure. (D) Optical images of 3D printed disc corresponding to Z0, Z1, and Z2 compositions. (E) Optical images of 3D printed scaffold corresponding to Z0, Z1, and Z2 compositions.

3.2. FTIR analysis

The FTIR spectra of the Z0, Z1, and Z2 scaffolds exhibited several characteristic absorption peaks corresponding to the chemical structure of the PU matrix (Fig. 3A). All groups showed a broad band near 3330 cm^{-1} associated with O–H stretching vibrations, and a strong peak at approximately 1725 cm^{-1} corresponding to C═O stretching of the urethane carbonyl group. Peaks near 2925 cm^{-1} and ∼1450 cm^{-1} were attributed to C–H stretching and bending vibrations, respectively.[25,26] Upon increasing the ZnO content, the overall spectral profile remained largely consistent, indicating the preservation of the PU chemical backbone across all formulations. However, the Z1 and Z2 groups exhibited enhanced intensities in the 1000–1100 cm^{-1} region.

3.3. Crystallographic characterization by XRD

The XRD patterns of the Z0, Z1, and Z2 scaffolds are shown in Fig. 3B. No sharp diffraction peaks were observed for Z0, indicating the absence of crystalline domains in the base formulation. Upon incorporation of ZnO nanoparticles, both the Z1 and Z2 groups displayed well-defined diffraction peaks superimposed on the polymer background. These peaks appeared at 2θ values of approximately 31.8° and 36.3°, corresponding to the (100) and (101) planes of hexagonal wurtzite ZnO (JCPDS no. 36-1451), respectively. The intensity of these peaks increased with increasing ZnO content, with Z2 exhibiting the most prominent signal intensity. No peak broadening or shifting was observed.

3.4. Surface wettability characterization

Water contact angle measurements demonstrated a gradual decrease in surface hydrophobicity with increasing ZnO content

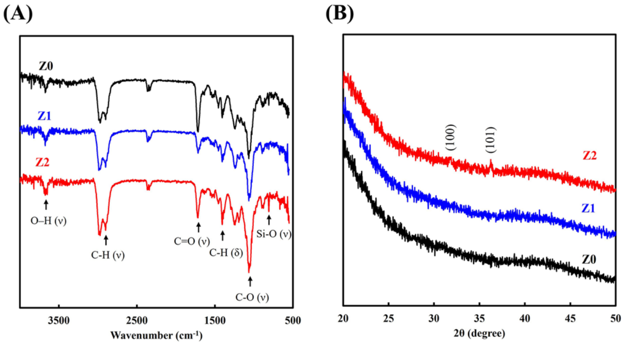

Fig. 3 (A) FTIR spectra of PU scaffolds prepared with different ZnO contents. (B) XRD patterns collected from Z0, Z1, and Z2 groups.

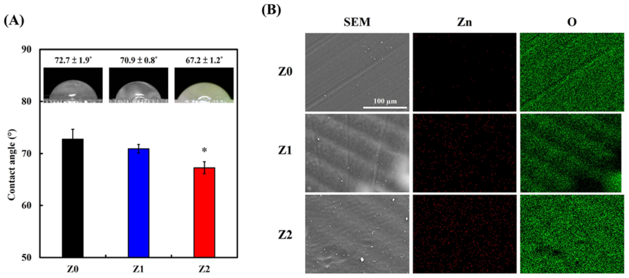

Fig. 4 (A) Contact angle measurements of PU scaffold surfaces with inset droplet profiles. (B) SEM micrographs and EDX elemental maps of Zn and O for Z0, Z1, and Z2 surfaces. * indicates statistically significant differences compared to Z0 ($p < 0.05$). Data represent the mean ± SD of 6 measurements.

in the PU scaffolds (Fig. 4A). The Z0 group exhibited an average contact angle of 72.7 ± 1.9°, indicative of the moderately hydrophilic nature of the PU/HEMA base resin. Upon incorporation of ZnO, the contact angle decreased slightly to 70.9 ± 0.8° in Z1, and more significantly to 67.2 ± 1.2° in Z2, with the reduction in Z2 being statistically significant ($p < 0.05$).

3.5. Surface morphology and elemental mapping

The surface morphologies and elemental distributions of Z0, Z1, and Z2 scaffolds were analysed using SEM and EDX mapping (Fig. 4B). SEM images revealed that the Z0 scaffold surface was relatively smooth, consistent with the homogeneity of the neat PU/HEMA resin. In contrast, the Z1 and Z2 groups exhibited increasingly roughened surfaces with visible fine particulates, which became denser in Z2, corresponding to the higher ZnO content. EDX mapping confirmed the elemental presence and distribution of Zn and O. The Z0 group showed no detectable Zn signal, while both Z1 and Z2 exhibited clear Zn signals distributed across the scaffold surface. The Zn signal was denser and more uniformly distributed in Z2, in agreement with its higher filler loading. Meanwhile, the oxygen signal was homogeneously distributed in all groups, reflecting the consistent polymer background.

3.6. Compressive mechanical properties of as-printed scaffolds

Compressive testing of the as-printed Z0, Z1, and Z2 scaffolds revealed significant differences in mechanical performance as a function of ZnO content (Fig. 5). The Z0 group exhibited a compressive strength of 7.5 ± 0.7 MPa and a Young's modulus of 50.3 ± 4.6 MPa. Upon the incorporation of ZnO, both parameters increased in a concentration-dependent manner. The Z1 group showed improvements to 8.5 ± 0.5 MPa in strength and 60.8 ± 2.7 MPa in modulus, while the Z2 group exhibited the most pronounced enhancement, with a compressive strength of 11.5 ± 0.9 MPa and modulus of 66.2 ± 6.3 MPa.

3.7. Aging-induced alterations in crystallographic and chemical stability

The evolution of crystallinity in Z0, Z1, and Z2 scaffolds following 0 and 150 hours of accelerated aging is depicted in Fig. 6A. The Z0 samples, devoid of ZnO incorporation, exhibited the expected broad amorphous halo centered around 20°, characteristic of the disordered nature of the PU/HEMA matrix. This feature remained unaltered post-aging, indicating the absence of any thermally or UV-induced crystallization. Conversely, scaffolds containing ZnO nanoparticles (Z1 and Z2) displayed persistent and well-defined diffraction peaks at 2θ values near 31.8° and 36.3°, attributable to the (100) and (101) planes of the hexagonal wurtzite phase of ZnO. Notably, these peaks exhibited no appreciable broadening or attenuation following the 150-hour aging protocol, signifying the remarkable structural resilience of ZnO under synergistic UV and thermal stress.

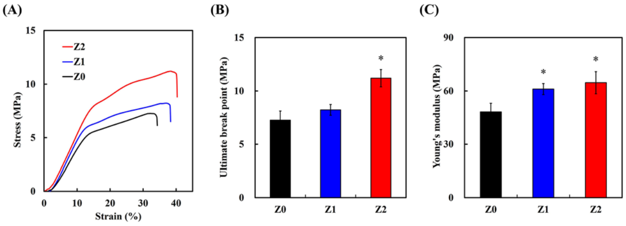

Fig. 5 (A) Compressive stress–strain curves of as-printed scaffolds. (B) Comparison of ultimate compressive strength. (C) Comparison of Young's modulus across different scaffold formulations. * indicates statistically significant differences compared to Z0 ($p < 0.05$). Data represent the mean ± SD of 6 measurements.

Fig. 6B presents the FTIR spectra for Z0, Z1, and Z2 scaffolds across aging intervals of 0, 50, 100, and 150 hours, revealing time-dependent chemical transformations in the polyurethane network. For Z0, a progressive diminution in the intensities of the N–H stretching (~3300 cm^{-1}) and C=O stretching (~1725 cm^{-1}) bands was evident, signifying the scission of urethane linkages and backbone degradation. Additionally, a pronounced broadening and intensification in the 1100–1000 cm^{-1} region suggested accumulation of ether and oxidative degradation products. These observations reflect advanced photothermal oxidative degradation, consistent with

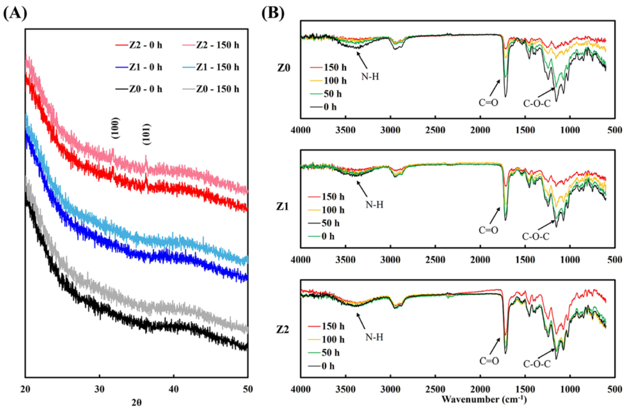

Fig. 6 (A) XRD patterns of PU scaffolds at 0 h and 150 h of accelerated aging. (B) FTIR spectra of Z0, Z1, and Z2 scaffolds at 0, 50, 100, and 150 h.

established PU aging mechanisms. In contrast, ZnO-containing groups exhibited attenuated chemical deterioration. While Z1 showed modest decreases in urethane-associated absorptions beyond 100 hours, Z2 maintained relatively stable peak profiles throughout the aging cycle.

3.8. Surface wettability after accelerated aging

Contrary to conventional expectations that aging typically enhances surface hydrophilicity through oxidation and polar group generation, the contact angle measurements in this study revealed a consistent increase in surface hydrophobicity across all groups. As illustrated in Fig. 7A, the Z0 scaffolds, composed of unfilled PU, exhibited an increase in contact angle from 72.7 ± 1.9° at 0 h to 88.0 ± 2.6° after 150 h of aging. Z1 and Z2 scaffolds demonstrated even greater changes, with Z1 increasing from 70.9 ± 0.8° to 91.5 ± 1.8° and Z2 from 67.3 ± 1.2° to 95.8 ± 2.2°, respectively. These temporal shifts were consistent across both bar chart data (Fig. 7B) and the time-resolved plot (Fig. 7C), which demonstrated statistically significant differences, particularly for ZnO-reinforced groups.

3.9. Compressive properties after accelerated aging

The compressive mechanical behavior of the PU-based scaffolds showed a progressive decline with increasing aging time; however, the magnitude of deterioration varied significantly depending on the ZnO content. As shown in Fig. 8A–C, the stress–strain curves for all groups flattened over time, with the most pronounced reduction in the Z0 group. Quantitatively, the Z0 scaffolds exhibited a marked drop in compressive strength from approximately 7.5 MPa at 0 h to 4.5 MPa at 150 h, and a corresponding decrease in Young's modulus from ∼50.3 MPa to ∼41.2 MPa. In contrast, the Z1 scaffolds, which contained 1 wt% ZnO, demonstrated a more gradual decline. Their compressive strength dropped from ∼8.3 MPa to ∼5.9 MPa, while the modulus decreased from ∼60.8 MPa to ∼50.2 MPa over the same aging period. Notably, the Z2 scaffolds showed the best aging resistance among all groups. While some decline was observed, from ∼11.5 MPa to ∼8.7 MPa in compressive strength and from ∼66.2 MPa to ∼58.9 MPa in modulus, these reductions were substantially less severe than those of Z0 and Z1. Additionally, to further evaluate environmental durability, freeze–UV alternating aging tests were conducted, where scaffolds underwent repeated cycles of freezing at −80 °C and subsequent UV exposure at room temperature. As shown in Fig. S2,† the ZnO-reinforced scaffolds, particularly Z2, maintained higher compressive strength and Young's modulus after freeze–UV cycles compared to the unfilled PU scaffold, demonstrating their improved resistance to extreme temperature fluctuations.

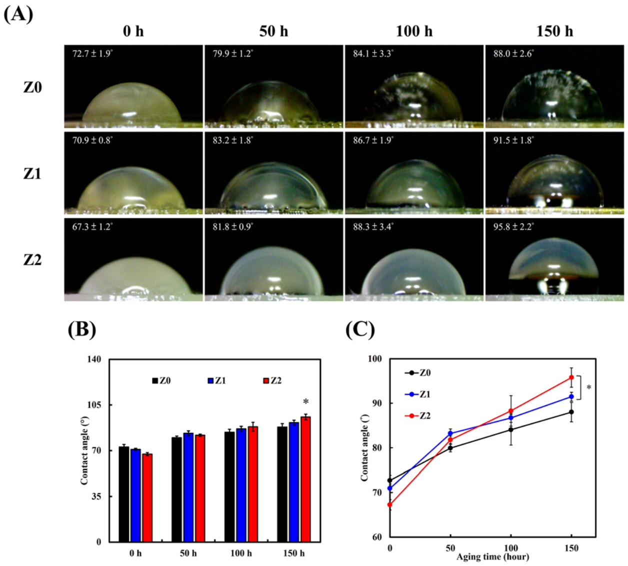

Fig. 7 (A) Water contact angle profiles of Z0, Z1, and Z2 scaffolds at different aging time points with corresponding droplet images. (B) Quantitative comparison of contact angle values at each time point. (C) Time-dependent contact angle changes. * indicates statistically significant differences compared to Z0 at the same time point ($p < 0.05$). Data represent the mean ± SD of 6 measurements.

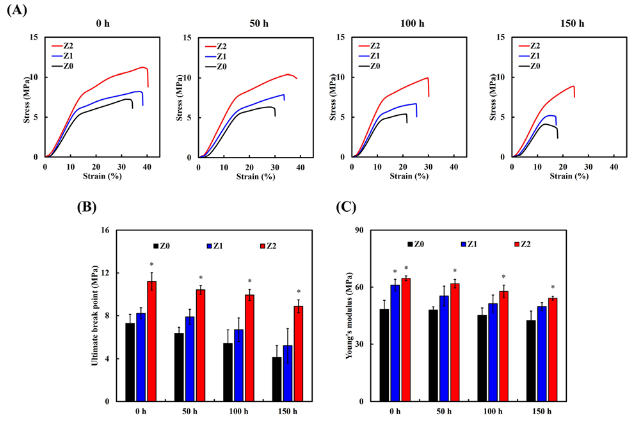

Fig. 8 (A) Compressive stress–strain curves of Z0, Z1, and Z2 scaffolds after 0, 50, 100, and 150 h of accelerated aging. (B) Comparison of ultimate compressive strength. (C) Comparison of Young's modulus. * indicates statistically significant differences compared to Z0 at the same time point ($p < 0.05$). Data represent the mean ± SD of 6 measurements.

3.10. Microstructural degradation after accelerated aging

SEM imaging of the scaffold surfaces at four time points (0, 50, 100, and 150 h) revealed progressive morphological deterioration in all groups, with marked differences in the extent and character of the damage (Fig. 9). In the Z0 group, micrographs showed that initially smooth surfaces at 0 h began to exhibit severe cracking and deep fissures as early as 50 h, which further propagated and widened with aging. By 150 h, extensive surface delamination, large interfacial gaps, and brittle fracture features dominated the morphology. The Z2 group displayed the most stable microstructure throughout the aging period. SEM images revealed only minimal surface erosion and rare microcracks, even after 150 h of aging. No significant fissures or delamination were detected, and the overall surface texture remained continuous and cohesive.

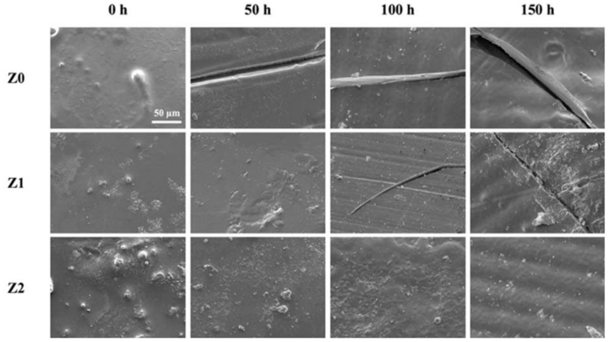

Fig. 9 SEM images of scaffold surfaces at 0, 50, 100, and 150 h of accelerated aging for Z0, Z1, and Z2. All micrographs were collected from representative regions; scale bar = 50 µm.

4. Discussion

The progressive whitening effect observed with increasing ZnO content was attributed to the intrinsically high refractive index and scattering behaviour of the ZnO nanoparticles dispersed within the polymer network, which effectively reduced light transmittance through the structure. Additionally, the steeper slopes in the shear stress–strain curves for Z1 and Z2 indicate enhanced resistance to shear deformation, likely due to filler-induced matrix stiffening and improved network entanglement. These physical changes set the stage for understanding the subsequent chemical and structural findings. Further supporting the successful incorporation of ZnO, the enhanced intensities observed in the 1000–1100 cm^{-1} region in Z1 and Z2 are associated with C–O and Si–O vibrations, likely originating from TMSPM incorporation.[20] These changes suggest improved interfacial interactions and confirm the successful inclusion of TMSPM-modified ZnO, without the appearance of new or unexpected peaks. The spectral differences remained subtle but consistent with previous studies involving silane-functionalised fillers, supporting stable chemical integration within the PU matrix. In line with the FTIR results, the emergence of ZnO-related diffraction peaks confirmed the successful incorporation of crystalline ZnO within the PU matrix without altering its native crystal structure. The gradual increase in the peak intensity with increasing ZnO concentration further supported the uniform distribution and stable integration of the nanoparticles in the bulk network. No peak broadening or shifting was observed, implying minimal stress-induced distortion of the ZnO lattice or crystal confinement effects within the polymer. These findings are consistent with previous reports on PU–ZnO nanocomposites prepared *via* light-curing techniques.[27] The XRD data corroborate the FTIR results, supporting the physical incorporation of ZnO into the matrix without disrupting the polymer backbone or triggering interfacial degradation.

On the level of surface properties, these results suggest a ZnO-induced increase in surface wettability, likely due to the hydrophilic characteristics of ZnO and its partial exposure at the scaffold surface. The trend aligns with the increased filler content and supports the notion that ZnO particles near or at the surface promote greater water spreading due to their polar surface groups. Although the magnitude of change was moderate, the results confirm a composition-dependent modulation of surface energy in the nanocomposite materials.[28] These observations confirm the effective incorporation and dispersion of ZnO within the PU matrix and the absence of severe nanoparticle agglomeration. The even distribution of ZnO supports its expected contribution to mechanical reinforcement and UV shielding throughout the bulk and surface regions of the scaffold. The increase in mechanical properties can be attributed to the reinforcing effect of ZnO nanoparticles, which act as rigid fillers that support load-bearing and reduce polymer matrix deformation. The enhancement is further supported by the presence of TMSPM, which promotes stronger interfacial bonding between ZnO and PU, improving stress transfer and limiting filler debonding under load.[20] These mechanical gains were achieved without compromising the integrity or print fidelity of the scaffolds, as previously confirmed by SEM and visual assessments. Furthermore, the SEM observations revealed periodic striations on the scaffold surfaces, which are attributed to the layer-by-layer curing process inherent to DLP printing. These surface textures result from the array-based digital micromirror device (DMD) projection system. Overall, the ZnO-reinforced PU scaffolds demonstrate tunable mechanical performance and are well suited for applications requiring lightweight yet durable structural components.[29]

Turning to aging behaviour, the data indicate that ZnO nanoparticles neither degrade nor undergo phase transitions under these conditions, thus preserving their reinforcing and UV-shielding capacities. This crystallographic invariance confirms ZnO's role as a durable and structurally stable filler phase within polymer matrices subjected to extended environmental exposure. The chemical resilience observed in Z2 is indicative of its superior stabilization, likely arising from ZnO's capacity to attenuate incident UV radiation and its potential to quench reactive oxidative species.[30] The limited evolution in the oxidative signature of Z2 further supports its effectiveness in suppressing secondary degradation reactions. Importantly, no emergent bands indicative of crosslinking, cyclization, or other side reactions were detected, suggesting that degradation was confined to classical scission and oxidation pathways. The XRD and FTIR analyses underscore the dual protective functionality of silane-functionalized ZnO nanoparticles in PU matrices.[31] These fillers not only retain their intrinsic crystallinity, ensuring continuous mechanical reinforcement and UV attenuation, but also play a pivotal role in preserving the molecular integrity of the polymer through radical quenching and photothermal shielding. The data strongly advocates for the integration of such nanostructured ceramic fillers in advanced polyurethane systems designed for sustained exposure to UV-intensive or thermally demanding operational environments. Interestingly, and contrary to conventional expectations, these results suggest that, instead of oxidation-driven surface activation, the dominant surface process under UV/thermal stress was morphological reconfiguration. Aging may have triggered reorientation or phase migration, whereby low-polarity segments (*e.g.*, urethane hard segments or silane-rich domains) reorganize at the surface.[32] This effect could be further promoted by ZnO, which may restrict chain mobility and favor the exposure of filler-rich, lower-energy interfaces. Additionally, UV-induced crosslinking or surface densification might have occurred, effectively sealing polar sites beneath a less reactive surface layer.[33] Although ZnO nanoparticles are inherently hydrophilic, the aged surfaces of ZnO-containing scaffolds exhibited increased contact angles. This may result from UV- and heat-induced surface restructuring, including reorientation of low-polarity segments or the formation of oxidized layers with reduced affinity for water. In the Z2 group, which contained the highest filler content, the surface presented the most consistent and elevated contact angle after aging, reflecting suppressed moisture interaction likely due to these surface changes rather than the inherent property of ZnO. Overall, the ZnO-containing PU scaffolds demonstrated strong resistance to surface wetting under environmental aging. This behavior reflects the complex interfacial dynamics governed by filler distribution, UV shielding, and molecular mobility. These findings challenge simplistic assumptions about aging-induced hydrophilicity and underscore the importance of integrating surface and mechanical analyses in evaluating long-term nanocomposite durability.[34]

The mechanical findings after aging complement the microstructural observations.[35,36] This degradation in Z0 is indicative of substantial structural breakdown due to chain scission, oxidative aging, and the absence of any UV-shielding filler phase. This intermediate performance suggests partial protection offered by ZnO, consistent with prior FTIR and XRD findings that indicated delayed molecular degradation and better retention of chemical functionality. However, the moderate decline also points to limitations in filler concentration and dispersion efficiency, especially near the surface, where aging effects tend to be more severe. The relatively high ZnO loading at 2 wt% likely contributed to several stabilizing effects, including enhanced UV attenuation, inhibition of radical-induced chain scission, and reduced moisture diffusion into the bulk material. These combined chemical and morphological stabilizing effects are considered to be the primary reasons Z2 retained mechanical integrity under prolonged thermal and UV exposure. These observations reinforce the conclusion that filler-enhanced scaffolds are more resistant to environmental degradation. The results highlight the superior aging tolerance of ZnO-reinforced PU systems, particularly when adequate nanoparticle loading is employed.[30,37] The Z2 formulation, in particular, shows promise for mechanically resilient applications in environments subject to UV and thermal cycling. These observations are consistent with pronounced chain scission, matrix embrittlement, and moisture-induced degradation, corroborating the results of FTIR and mechanical testing. In contrast, Z1 scaffolds exhibited a more gradual degradation profile. Minor surface roughening and localized crack formation were observed by 50 h, progressing to partial surface tearing and visible fissures along strut junctions by 100 and 150 h. The damage remained relatively confined, suggesting that the incorporation of 1 wt% ZnO moderately delayed the onset and propagation of microcracks. This protective effect is likely linked to the UV attenuation capacity of ZnO and partial suppression of oxidative chain scission. The enhanced morphological preservation in Z2 can be attributed to both the higher filler content and improved dispersion of ZnO nanoparticles. These ceramic nanofillers likely served as physical reinforcements that dissipated local stress, pinned crack tips, and hindered microvoid expansion. This effect aligns with the role of ZnO as both a UV stabilizer and a crack-arresting agent. Collectively, the SEM evidence underscores the structural advantage conferred by ZnO incorporation. Increasing the ZnO content reduced the density and severity of aging-induced defects, maintaining scaffold integrity under prolonged UV and thermal stress. These observations further support the conclusion that the durability of PU-based scaffolds is governed by both chemical and microstructural resilience, both of which are enhanced by nanoparticle reinforcement.

5. Conclusions

In this study, we developed a series of 3D-printed PU-based scaffolds reinforced with different concentrations of ZnO nanoparticles and stabilised them using the silane coupling agent TMSPM. Through systematic material characterisation, we demonstrated that the incorporation of ZnO significantly improved the physicochemical stability and mechanical performance of the scaffolds before and after accelerated aging. Initial characterisation revealed that increasing the ZnO content enhanced scaffold stiffness and compressive strength without compromising print fidelity. FTIR and XRD analyses confirmed the structural compatibility and chemical stability of the hybrid system, while SEM and contact angle measurements indicated uniform filler dispersion and surface wettability modulation. Under cyclic UV and thermal aging conditions, the ZnO-filled scaffolds exhibited superior resistance to degradation, as evidenced by their preserved chemical structure, minimal surface cracking, and the maintenance of mechanical integrity. These effects are attributed to the dual role of ZnO as a UV absorber and a mechanical crack-arresting agent, synergistically suppressing both chemical and physical aging pathways. Overall, the PU/TMSPM–ZnO system presented herein offers a robust and scalable strategy for fabricating lightweight, durable, and environmentally resilient polymer components *via* DLP-based 3D printing. The improved aging resistance and structural integrity highlight its potential for deployment in high-performance applications, such as automotive, aerospace, and outdoor infrastructure materials, where long-term stability under harsh conditions is critical.

Data availability

The data supporting this article have been included as part of the ESI.†

Author contributions

C.-C. T. and Y.-H. L. methodology, validation, investigation, formal analysis, writing – original draft, preparation, and writing – review & editing; Y.-H. L. helped with data analysis and interpretation; Y.-W. C. and F.-M. W. conceptualization, funding acquisition, project administration, and writing – review & editing.

Conflicts of interest

The authors declare no conflict of interest.

Acknowledgements

The authors acknowledge receipt grants from the Ministry of Science and Technology (MOST 113-2321-B-039-008 and 113-2811-E-039-001).

Notes and references

1 Y. C. Chiu, Y. H. Lin, Y. W. Chen, T. Y. Kuo and M. Y. Shie, *J. Mater. Chem. B*, 2023, **11**, 4666–4676.

2 M. Simonelli, Y. Y. Tse and C. Tuck, *Mater. Sci. Eng., A*, 2014, **616**, 1–11.

3 Z. X. Khoo, J. E. M. Teoh, Y. Liu, C. K. Chua, S. Yang, J. An, K. F. Leong and W. Y. Yeong, *Virtual Phys. Prototyp.*, 2015, **10**, 103–122.

4 Y. W. Chen, Y. H. Lin, C. C. Ho, C. Y. Chen, M. H. Yu, A. K. X. Lee, S. C. Chiu, D. Y. Cho and M. Y. Shie, *Biofabrication*, 2024, **16**, 045035.

5 H. Shi, Y. Li, K. Xu and J. Yin, *Mater. Today Bio*, 2023, **23**, 100799.

6 M. Zanon, R. Cue-López, E. Martínez-Campos, P. Bosch, D.-L. Versace, H. Hayek, N. Garino, C. F. Pirri, M. Sangermano and A. Chiappone, *Addit. Manuf.*, 2023, **69**, 103553.

7 Y. Wu, Q. Cao, Y. Wang, Y. Liu, X. Xu, P. Liu, X. Li, X. Zhu and X. Zhang, *Mater. Des.*, 2023, **233**, 112230.

8 J. J. Lee, H. Y. Ng, Y. H. Lin, E. W. Liu, T. J. Lin, H. T. Chiu, X. R. Ho, H. A. Yang and M. Y. Shie, *Biomater. Adv.*, 2022, **142**, 213132.

9 K. C. Cheng, Y. M. Sun and S. Hsu, *J. Mater. Chem. B*, 2023, **11**, 3592.

10 A. Sanati, A. Kefayat, M. Rafienia, K. Raeissi, R. S. Moakhar, M. R. Salamat, S. Sheibani, J. F. Presley and H. Vali, *Mater. Des.*, 2022, **221**, 110955.

11 Y. Wang, R. Liang, J. Lin, J. Chen, Q. Zhang, J. Li, M. Wang, X. Hui, H. Tan and Q. Fu, *J. Mater. Chem. B*, 2021, **9**, 7979–7990.

12 M. Cui, Z. Chai, Y. Lu, J. Zhu and J. Chen, *Resour. Chem. Mater.*, 2023, **2**, 262–276.

13 J. O. Akindoyo, M. D. H. Beg, S. Ghazali, M. R. Islam, N. Jeyaratnam and A. R. Yuvaraj, *RSC Adv.*, 2016, **6**, 114453–114482.

14 Z. Huang, Y. Wan, X. Zhu, P. Zhang, Z. Yang, F. Yao and H. Luo, *Mater. Sci. Eng., C*, 2021, **123**, 111967.

15 A. M. E. Saeed, M. A. El-Fattah and A. M. Azzam, *Dyes Pigm.*, 2015, **121**, 282–289.

16 G. Jerlin, B. R. Wiston and M. Ashok, *Mater. Sci. Eng., B*, 2025, **317**, 118210.

17 S. Raha and Md. Ahmaruzzaman, *Nanoscale Adv.*, 2022, **4**, 1868–1925.

18 C. Y. Chen, M. Y. Shie, A. K. X. Lee, Y. T. Chou, C. Chiang and C. P. Lin, *Biomedicines*, 2021, **9**, 907.

19 X. T. Dam, P. H. Dao, A. H. Nguyen, T. T. G. Pham, T. H. Nguyen, T. C. Nguyen, T. N. L. Ly and H. Thai, *J. Appl. Polym. Sci.*, 2024, **141**, e55466.

20 J. Xue, R. Han, Y. Li, J. Zhang, J. Liu and Y. Yang, *J. Mater. Sci.*, 2023, **58**, 14255–14283.

21 P. Meti, D. B. Mahadik, K.-Y. Lee, Q. Wang, K. Kanamori, Y.-D. Gong and H.-H. Park, *Mater. Des.*, 2022, **222**, 111091.

22 V. G. Parale, T. Kim, H. Choi, V. D. Phadtare, R. P. Dhavale, K. Kanamori and H. Park, *Adv. Mater.*, 2024, **36**, e2307772.

23 D. Duraccio, P. P. Capra and G. Malucelli, *Micro Nano Eng.*, 2024, **23**, 100266.

24 C. C. Tung, Y. H. Lin, Y. W. Chen and F. M. Wang, *Polymers*, 2023, **15**, 3744.

25 M. P. Mani, S. K. Jaganathan and E. Supriyanto, *Polymers*, 2019, **11**, 1323.

26 X. Wang, Y. Pei, Y. Hou and Z. Pei, *Polymers*, 2019, **11**, 313.

27 S. Zafar, R. Kahraman and R. A. Shakoor, *Eur. Polym. J.*, 2024, **220**, 113421.

28 Y. H. Lin, Y. Chen, E. W. Liu, M. C. Chen, M. H. Yu, C. Y. Chen, C. C. Ho, T. Y. Hsu-Jiang, J. J. Lee, D. Y. Cho and M. Y. Shie, *J. Nanobiotechnol.*, 2025, **23**, 45.

29 C. Wang, J. Zhang, J. Chen, J. Shi, Y. Zhao, M. He and L. Ding, *Int. J. Biol. Macromol.*, 2022, **208**, 97–104.

30 E. L. Irede, R. F. Awoyemi, B. Owolabi, O. R. Aworinde, R. O. Kajola, A. Hazeez, A. A. Raji, L. O. Ganiyu, C. O. Onukwuli, A. P. Onivefu and I. H. Ifijen, *RSC Adv.*, 2024, **14**, 20992–21034.

31 A. R. Hegde, M. U. Kunder, M. Narayanaswamy, S. Murugesan, S. C. Furtado, B. B. Veerabhadraiah and B. Srinivasan, *Environ. Sci. Pollut. Res.*, 2024, **31**, 38061–38082.

32 B. X. Cheng, W. C. Gao, X. M. Ren, X. Y. Ouyang, Y. Zhao, H. Zhao, W. Wu, C. X. Huang, Y. Liu, X. Y. Liu, H. N. Li and R. K. Y. Li, *Polym. Test.*, 2022, **107**, 107489.

33 J. Deng, L. Wang, L. Liu and W. Yang, *Prog. Polym. Sci.*, 2009, **34**, 156–193.

34 Y. Ma, X. Niu, X. Wang, X. Min, X. Wang and X. Guo, *Chem. Eng. J.*, 2025, **516**, 163985.

35 M. Arana, E. Ukar, I. Rodriguez, D. Aguilar and P. Álvarez, *Mater. Des.*, 2022, **221**, 110974.

36 Z. Wang, M. Wang, Y. Li, H. Xiao, H. Chen, J. Geng, X. Li, D. Chen and H. Wang, *Mater. Des.*, 2021, **203**, 109618.

37 R. Randis, D. B. Darmadi, F. Gapsari, A. A. Sonief, E. D. Akpan and E. E. Ebenso, *J. Mol. Liq.*, 2023, **390**, 123067.